Investigation on the structural and microstructural properties of copper-doped hydroxyapatite coatings deposited using solution precursor plasma spraying

Romnick Unabia, Simon Bonebeau, Rolando Candidato, Jenny Jouin, Olivier Noguera, Lech Pawlowski

Investigation on the structural and microstructural properties of copper-doped hydroxyapatite coatings deposited using solution precursor plasma spraying

Romnick B. Unabia[*1,2], Simon Bonebeau[2], Rolando T. Candidato, Jr.[1], Jenny Jouin[2], Olivier Noguera[2], and Lech Pawłowski[2]

[1] Physics Department, College of Science and Mathematics, MSU-Iligan Institute of Technology, A. Bonifacio Avenue, Tibanga, 9200, Iligan City, Philippines

[2] IRCER UMR 7315 CNRS, Université de Limoges, 12 Rue Atlantis, 87068 Limoges Cedex, France

*****Correspondence: romnickunabia@gmail.com; Tel.: + (33) (0) 587 50 24 00

ABSTRACT

Structural and microstructural investigation on solution precursor plasma sprayed copper-doped hydroxyapatite (Cu-HA) coatings with0, 3, 5 and 10 weight percent (wt.%) of Cu dopant concentration is presented. Scanning electron micrographs show no significant morphological changes at the surface and cross-section of the coatings as copper content increases. X-ray diffraction results show decreases in the HA phase content from 93% to 14% and degree of crystallinity form 94% to 85% along with the increase of impurity phases upon increasing the copper concentration. RAMAN and IR spectra depicted broadening and red-shifting of the phosphate bands due to the distortion of the HA structure induced by the insertion of the copper ions into the HA lattice. X-ray photoelectron spectroscopy results identified that the copper species incorporated in HA structure was Cu^{+} and Cu^{2+} ions. Incorporation of copper ions into HA was associated to an interstitial insertion along hexagonal channel of the HA structure which leads to the increase in the lattice *a* parameter and expansion of the unit cell volume observed in Rietveld refinement measurements. The insertion was induced by the dehydroxylation process of HA due to the high temperatures of the plasma jet. Furthermore, the dopant concentration limitation in order to maintain the dominance of HA phase in the coating is 5 wt.% of Cu.

Keywords: copper-doped hydroxyapatite, solution precursor plasma spray, microstructure investigation, interstitial insertion

1. INTRODUCTION

The occurrence of implant associated infection has been one of the major problems in biomedical application [1-3]. Hence, development of novel implants with inherent antibacterial capability is highly needed. This capability may be developed by the addition of metal ions to hydroxyapatite, $Ca_{10}(PO_4)_6(OH)_2$, (HA). The latter has been one important biomaterial for implants due to its biocompatibility and bioactivity [4-**Erreur ! Source du renvoi introuvable.**]. HA has an advantage of having a flexible structure that provides good absorption matrix for other ions in its lattice to add some biofunctionality such as antibacterial capability [3,6-8].

This present study focuses on the incorporation of copper ions to HA as it exhibits antibacterial characteristics, and has been found out to have pro-angiogenic potential, i.e. the ability to stimulate the formation of new blood vessels which increases the viability of bone-forming cells into implants [7-13]. However, the utilization of Cu is potentially toxic to humans if exceeds certain amounts [14-15]. Aside from that, incorporation of other ions in the HA structure bring about structural change which then could influence its physico-chemical properties [3, 8, 17].

In our previous paper [18], we presented the optimization of spray parameters to obtain Cu-HA coatings using SPPS process. The present contribution focuses on the structural and microstructural influence of various copper ion concentration in the HA matrix. Moreover, the possible mechanism on the incorporation of Cu ion into the HA structure will also be discussed in this study.

2. Experimental details

2.1. Solution preparation

For the preparation of Cu-doped calcium phosphate solution, copper nitrate trihydrate (*$Cu(NO_3)_2 \cdot 3H_2O$,Scharlau Lab., Barcelona, Spain, 99.5% purity*) was used as copper ion source, calcium nitrate tetrahydrate (*$Ca(NO_3)_2.4H_2O$, Scharlau Lab., Barcelona, Spain, 99% purity*) as calcium ion source and triethylphosphite (*$P(OEt)_3$, Sigma Aldrich, Saint-Louis, Missouri, USA, 97.5 % purity*) as phosphorous ion source. Deionized water was used as solvent in all preparations. After dissolving the *Ca* and *Cu* ions precursors, the solution was thoroughly mixed first using magnetic stirring before adding the hydrolyzed tri-ethyl phosphite solution as *P* ions precursor. The possible synthesis mechanism of all chemical precursors was discussed elsewhere [18]. The stoichiometry of final solution precursor was maintained to have atomic ratio [$(Ca + Cu)/P$] = 1.67. Finally, the mixed solution were continually stirred for 24 hours and left at ambient temperature for 5 days before plasma spraying. The samples' codes according to Cu concentration are pure HA for 0 wt.% Cu, 3% Cu-HA for 3 wt.% Cu, 5% Cu-HA for 5 wt.% Cu and 10% Cu-HA for 10 wt.% Cu.

2.2 Plasma spray parameters

SG-100 torch *(Praxair S.T., Indianapolis, IN, USA)* mounted on a 6-axis ABB IRB 140 industrial robot *(Zürich, Switzerland)* was used for plasma spraying of Cu-HA coatings. Argon gas with flow rate of 45 slpm (standard liter per minute) and hydrogen gas with flow rate of 5 slpm were used as primary and secondary gases, and were kept constant throughout all spraying experiment. The flow rate of solution was equal to 53 mL/min. The solution was injected into the plasma jet using mechanical injection system using an external injector (nozzle) with diameter of 0.3 mm. The injector was set under the angle of 30^o backwards with respect to the torch axis. The substrate used were stainless steel cylinders (ϕ = 25 mm, thickness = 3.0 mm). They were sandblasted using F36 alumina sand. The spraying distance was 50 mm. A rectangular spray pattern with 3.0 mm off-set distance after each spray scan at a speed of 500mm/s was used to spray. The temperature at the surface of the sprayed coating was

monitored using Impac IN 5 pyrometer (*LumaSense Technologies, Santa Clara, California, USA*).

2.3 Coatingscharacterization

The morphological features of the as-deposited Cu-HA at the surface and cross-section were observed using JEOL JSM-IT300LV (Massachusetts, USA) scanning electron microscope (SEM).

X-ray diffraction measurements were performed using a Bragg Brentano D8 Advance *(Brucker, Massachusetts, USA)* diffractometer with CuK_{α} radiation. The scans were performed in the range of 20° to 70° (2θ), with a step increment of 0.014°. The measured diffractograms were analyzed using Diffrac+EVA software with the JCPDS-ICDD database for the crystalline phase identification. TOPAS v.4.2 [19] software was used to estimate the relative amount (wt.%) of the crystalline phases present in the coating. The degree of crystallinity of the coating were determined using the following equation

$$Percent\ crystallinity, \% = \frac{I_{(300)} - V_{(112/300)}}{I_{(300)}} \times 100\% \qquad \text{(Eq. 1)}$$

where $I_{(300)}$ is the intensity at (300) peak and $V_{(112/300)}$ is the intensity of a valley between (112) peak and (300) peak [20, 21].

The average crystallite sizes of the coatings are calculated using Williamson-Hall plot method given in equation 2:

$$\frac{\beta \cos\theta}{\lambda} = \varepsilon\left(\frac{2\sin\theta}{\lambda}\right) + \frac{1}{\tau} \text{(Eq. 2)}$$

Where β is the integral broadening of the peaks in radians, θ is the Bragg angle, λ is the wavelength of the radiation, τ is the effective crystallite size and ε is the effective strain [21-22]. The planes used for the calculations are (002), (211), (112), (300), (202), (310), (222) and (213).

Due to the abundant presence of peaks, the unit cell refinement of the HA phase was performed using a full pattern matching with the Rietveld method [21] using JANA 2006 software [24]. In all cases, the refinements were performed using the phases observed including the impurities present in the samples. The structural models used for the refinement of the coatings' phases are listed in Table 1. In every case, the continuous background was modeled with a 10 terms Legendre polynomial function and the vertical position of the sample was refined. The peak profiles were represented by pseudo-Voigt functions. The cell parameters and profile parameters of the main phases were refined, while the cell parameters of the impurities were kept to their original values and their profile parameters were set to reasonable values and not refined.

Table 1. Structural models used for Rietveld refinements.

Phases		**Powder Diffraction File No.**	**References**
Name and notation in paper	**Chemical Formula**		
Hydroxyapatite,(HA)	$Ca_{10}(PO_4)_6(OH)_2$	09-0432	[25]
Alpha-tricalcium phosphate,(α-TCP)	$Ca_3(PO_4)_2$	09-0348	[26]
Tetracalcium phosphate (TTCP)	$Ca_4P_2O_9$	25-1137	[27]
Calcium copper phosphate (CCP)	$Ca_{19}Cu_2(PO_4)_{14}$	46-0403	[28]
Calcium oxide (Lime)	CaO	37-1497	[29]
Copper oxide (Tenorite)	CuO	48-1548	[30]

The infrared characteristicsof the Cu-HA coatings were determined by Attenuated Total Reflectance – Fourier Transform Infrared (ATR–FTIR) spectroscopy using Nicolet 6700 *(Thermofisher, Massachusetts, USA)* spectrometer with a scan range at 4,000- 400 cm^{-1} infrared

spectral region having 2 cm^{-1} resolution over 32 scans. All experimental runs were conducted at room temperature and the reflection data were converted into absorption mode.

The experimental Raman spectra of the coatings were recorded at room temperature using an Invia Reflex Renishaw (Wotton-under-Edge, United Kingdom) Raman spectrometer equipped with a laser diode (λ=785 nm, 30 mW) in a backscattering geometry using a 100x objective lens. Prior to measurement, the spectrometer was calibrated with a standard silicon sample. The scattered photons from the sample were dispersed in a 1200 lines/mm grating and collected at the same time on a charge coupled device camera detector. The spectra were obtained in the 75-1200 cm^{-1} spectral range using a microprobe spot size of 2.0 µm and spectral resolution of 2.0 cm^{-1} with 10 seconds exposure time. Raman maps (400x400 μm^{-2}) were collected using the SteamLine mode (each line is 40 µm long and 1 µm large) with 5 seconds exposure time and a 20x objective lens. For each map a total of 1349 spectra was collected.

The amount of *Ca*, *P* and *Cu* in the coatings were quantitatively measured using Optima 8300 DV Inductive coupled plasma – atomic emission spectroscopy (ICP-AES) (Perkin Elmer, Wellesley, Massachusettes, USA). The coatings are first processed into a solution by dissolving the dried scraped-off coatings with nitric acid and submitted to microwave oven. The solution is then nebulized inside the chamber and is ionized by ICP torch. The photons emitted were then measured as concentration of analyzed atoms (*Ca*, *P* and *Cu*) in mg/L.

X-ray photoelectron spectroscopy (XPS) characterization was carried out to determine the surface chemical composition using Surface Science Instruments X-Probe and S-probe spectrometers. XPS irradiates the sample with a penetration depth of 8-10 nm using a monochromatic Al Kα X-ray sources ($h\nu$ = 1486.6 eV) causing the emission of photoelectrons and Auger electrons which are identified by hemispherical analyzers and multichannel detectors. The information gathered through XPS was used in the determination of the number and kinds of atoms according to its energies in the spectral peaks.

3. Results

3.1. Microstructural properties of Cu-HA coatings

The surface morphology of the coatings with different Cu concentrations display the characteristic deposits of solution precursor plasma spray (SPPS) process (see Figure 1) which shows agglomerated and melted particles with fine spherical particles (less than 1 µm sizes). The surface of the coatings revealed a cauliflower-like morphology. Relatively dense microstructure with cone-tip defect and micropores were observed at the cross-section of Cu-HA coatings. There are no particular changes of the coatings' microstructures with the copper concentration.

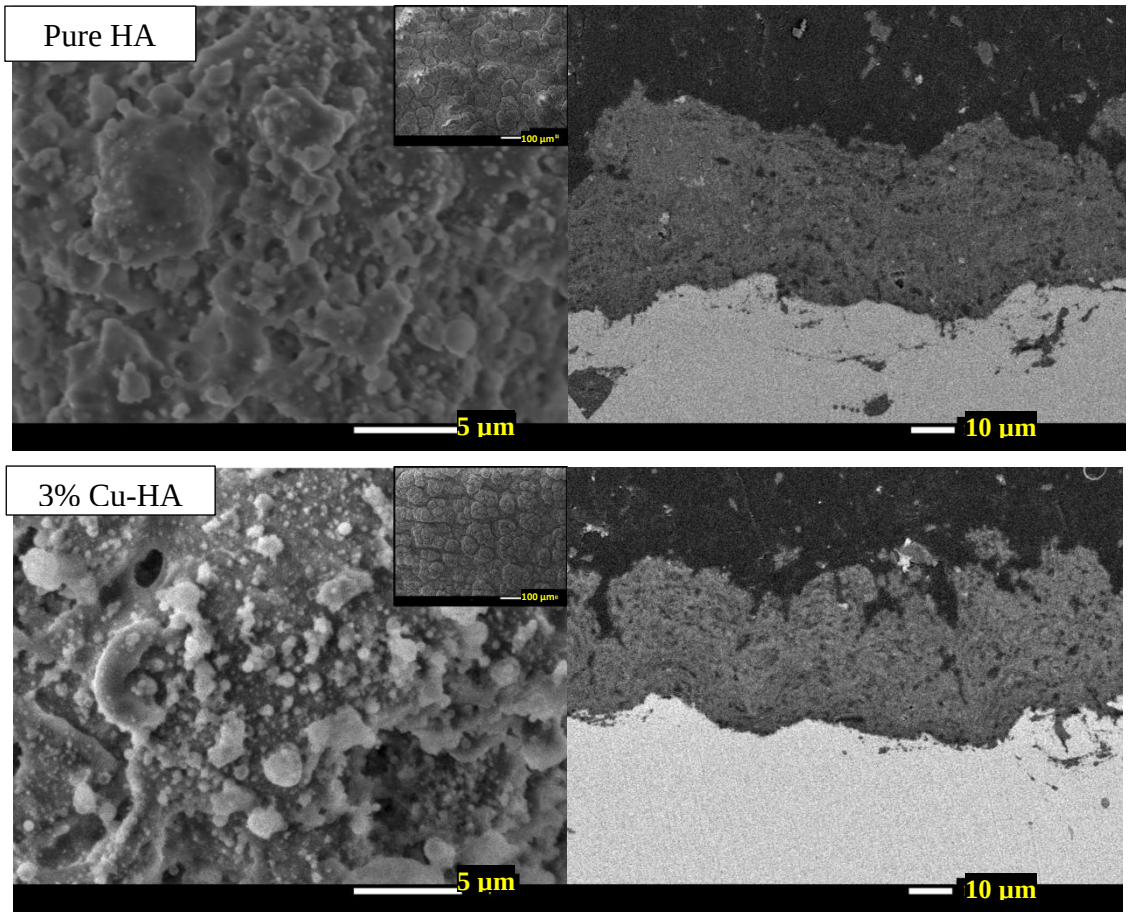

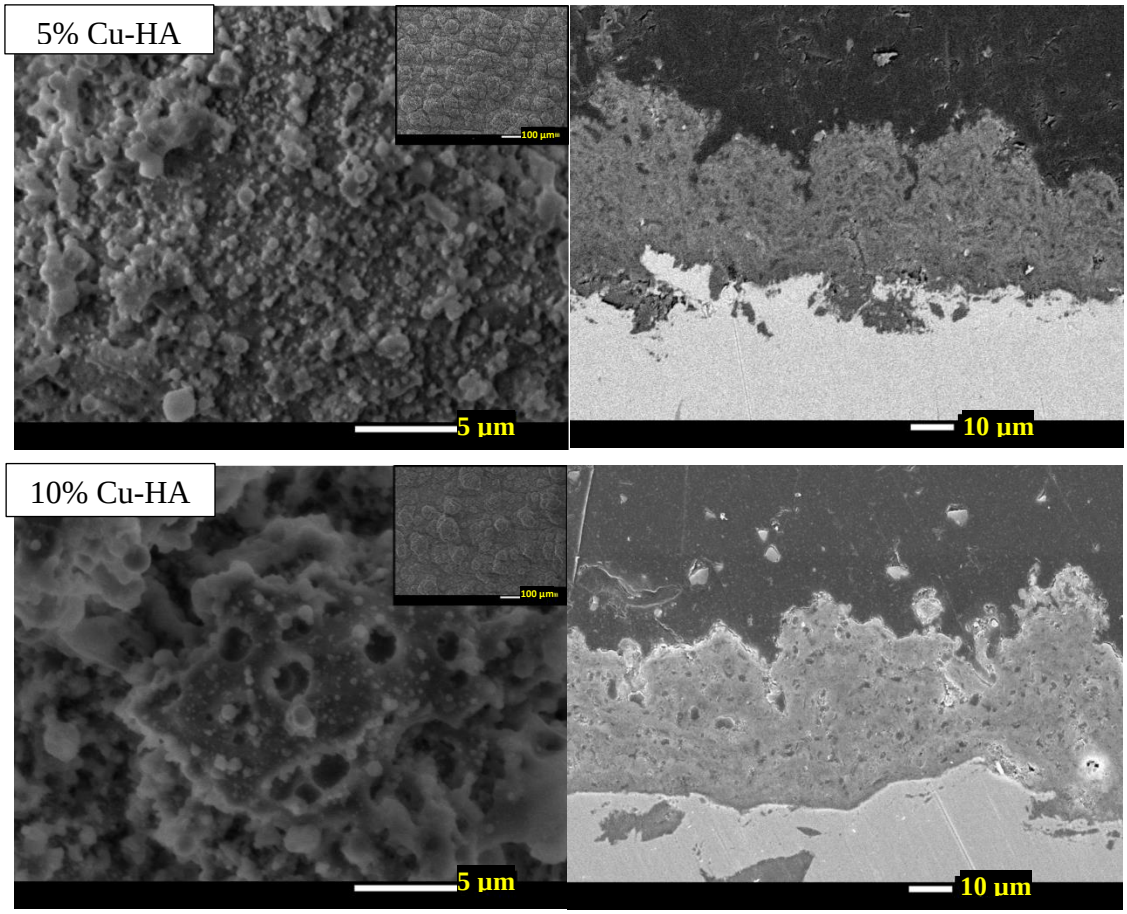

Figure 1 SEM images at the surface and cross-section of SPPS pure HA, 3%Cu-HA, 5%Cu-HA and 10% Cu-HA coatings; inset: low magnification at the surface.

3.2. Phase identification of the coatings

The XRD diagrams of the coatings were analyzed using TOPAS software to identify the crystalline phase formation during the process. The phase identification of all samples is shown in Figure . The coatings sprayed without copper dopant were mainly composed of 93 wt.% HA. However, presence of TTCP (6 wt.%) and CaO (1wt.%) as minor impurities were observed as decomposition product of HA at high temperatures. The coatings doped with 3 wt.% Cu shows HA as the dominant phase having 88 wt.%, but with some α-TCP (9 wt.%), tenorite CuO (2 wt.%), and very small traces of CaO (<1 wt.%) were also identified. The presence of CuO in the coatings may be attributed either to the decomposition of copper nitrate precursor or the reaction of copper ions with oxygen in HA structure at high temperatures. The coating having composition of 5 wt.% Cu in the HA matrix shows the quantity of HA phase of 81 wt.%. The

phases of β-TCP (9 wt.%), α-TCP (8 wt.%) and traces of tenorite (2wt.%) were also observed. For 10% Cu-HA coating, α-TCP becomes the dominant phase with 71 wt.% while HA phase was only 14 wt.%. The phases ofβ-TCP (11 wt.%) and CaO (2 wt.%), and CuO (1 wt.%) were observed. The traces of calcium copper phosphate CCP phases were observed at high dopant concentration. The latter will not be considered in further discussion.

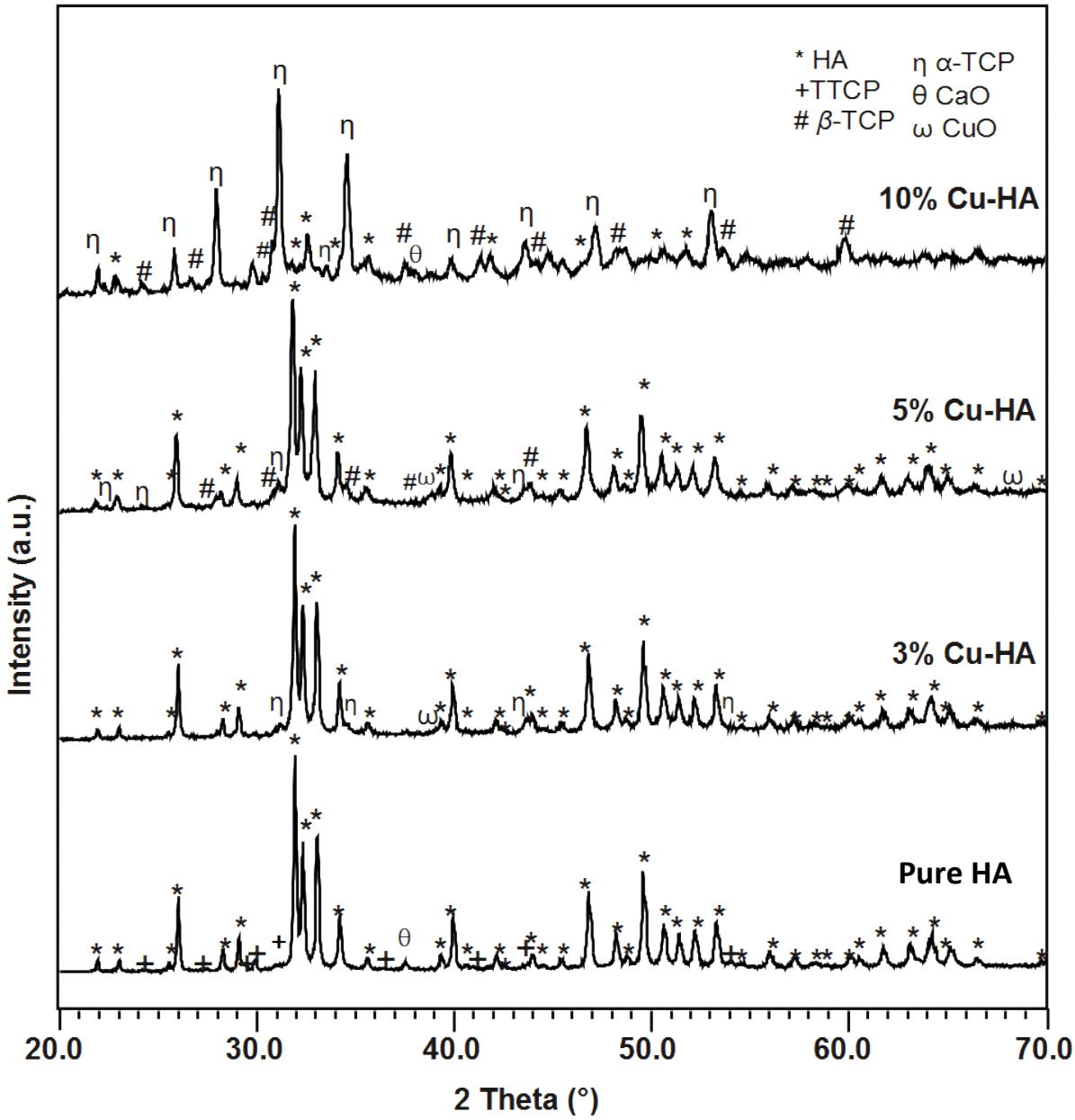

Figure 2: X-ray diffraction diagrams of the coatings with 0 wt.%, 3 wt.%, 5wt.% and 10 wt.% Cu showing HA and impurities depending on the Cu concentration.

The calculation of the degree of crystallinity shows values in decreasing order from 94% for pure HA, 90% for 3%Cu-HA and 85% for 5%Cu-HA which correlates to the increasing

presence of impurities that could distort the HA structure. The obtained crystallinity of coatings was still suitable for biomedical applications as ISO standard requires at least 45% crystallinity for HA coatings [31]. The average crystallite sizes obtained using Williamson-Hall method were equal to 100 nm for pure HA, 118 nm for 3% Cu-HA and 83 nm for 5% Cu-HA which lies in the size range considered as nanomaterials which mimics the biological apatite, i.e., essential for bioactivity during implantation [32-33].

3.3. Rietveld refinement

Unit cell refinement was performed by a full pattern matching method to clarify the incorporation of copper into the HA structure using JANA 2006 software. Due to the large number of crystalline phases in the sample, the refinement was focused on the main crystalline phase. The impurities were taken into account in the calculation but their characteristics were not refined due to the small intensity of their respective peaks. The obtained results are summarized in Table , along with the parameters from bulk HA. When comparing the standard values from bulk, i.e., prepared via conventional synthesis method, the volume of the unit cell of the pure HA coating synthesized by plasma spraying was significantly lower which could be due to compressive stress induced by the substrate or the result of residual constraints from the very high temperature used during the spraying.

However, when comparing the results of the refinements for the different coatings, we can notice a clear increase of the volume of the unit cell with the addition of Cu. The expectation that Cu substitutes to Ca sites in HA structure was not probable because, if there were substitutions, the volume would tend to decrease due significant difference in the ionic radii of the two species ($r(Ca^{2+})$=1.00 Å and $r(Cu^{2+})$=0.73 Å) [34]. Moreover, the lattice parameters *a* and *c* of the HA increased of very similar quantities with the addition of 3% Cu, while for 5% Cu, the lattice parameter a seems to be the most affected. Considering these observations, copper ion is probably inserted in the HA structure in interstitial positions along the hexagonal

channel. In connection to this claim, related studies on Cu-doping into HA had also described that the insertion mechanism copper ions is at the interstitial 2b Wyckoff site which leads to the formation of the linear oxocuprate O-Cu-O entities along the hexagonal channel [7, 35-37].

Table 2: Refined unit cell parameters and volume, goodness of fit, reliability factors and evolution of unit cell parameters for the HA phase.

	HA standard	Pure HA	3%Cu-HA	5%Cu-HA	10%Cu-HA
Lattice parameters					
a (Å)	9.432	9.4163(2)	9.4229(2)	9.4280(3)	NR
c (Å)	6.881	6.8829(2)	6.8893(2)	6.8877(2)	NR
V ($Å^3$)	530.72	528.53(2)	529.75(2)	530.21(3)	NR
Refinement factors					
GOF	-	1.38	1.56	1.25	-
Rp (%)	-	4.62	4.28	2.86	-
Rwp(%)	-	6.59	6.78	3.99	-
Percent difference with respect to pure HA					
a	-	-	0.07	0.12	-
c	-	-	0.09	0.07	-
Volume	-	-	0.23	0.32	-

Note: numbers in parenthesis represent the standard deviations.
NR- not refined

3.4. Attenuated Total Reflectance-Fourier Transform Infrared (ATR-FTIR) Spectroscopy

Figure 3 shows the FTIR spectra of coatings with different copper concentrations. The bending vibration of the phosphate P-O modes at 500-600 cm^{-1} and the symmetric and asymmetric vibration of the phosphate at 900-1200 cm^{-1} were observed in all coatings. In addition, the OH of HA lattice can be observed as a shoulder peak at ~630cm^{-1} and the stretching vibration of OH of HA centered at 3571 cm^{-1} indicating the formation of the hydroxyapatite material is depicted on all coatings. Broadening and red-shifting of peaks were observed with increasing copper concentration in the coatings, signifying the presence of distortions induced by the incorporation of copper ions into the HA structure. Moreover, this could also be attributed to the increasing impurity phases in relation to the XRD results.

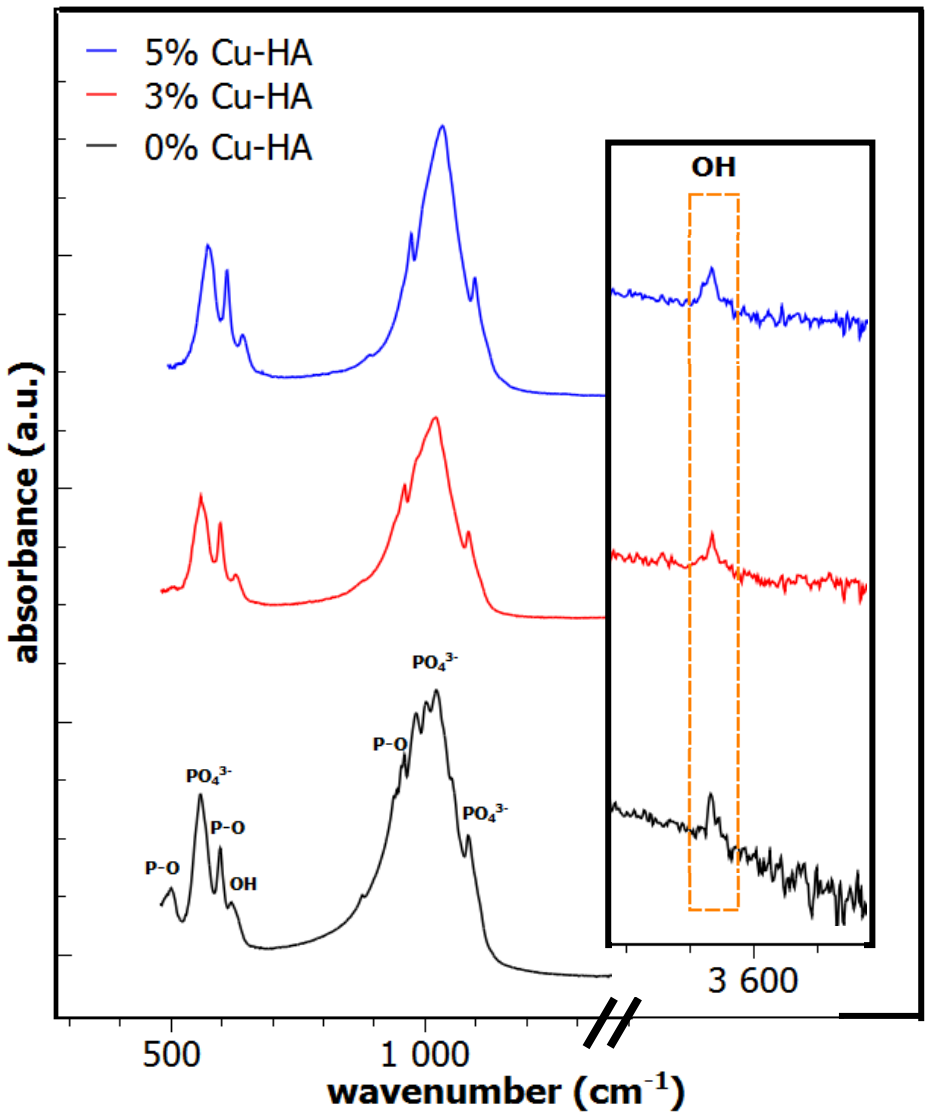

Figure 3: FTIR absorption spectra of SPPS HA with different copper concentration; the OH peaks (left side) were zoomed in for better observation.

3.5. Raman spectroscopy

The Raman analysis of the pure HA, 3% Cu-HA and 5% Cu-HA coatings is presented in Figure 4. In the pure HA coating spectra, the observed bands wherein the 428 cm^{-1} and 447 cm^{-1}associated to the ν_2 PO_4^{3-} degenerate bending modes, 580 cm^{-1}, 590 cm^{-1} and 607 cm^{-1} attributed to the ν_3 PO_4^{3-} asymmetric bending modes, and 1029 cm^{-1}, 1047 cm^{-1} and 1076 cm^{-1} assigned to the ν_4 PO_4^{3-} asymmetric stretching modes indicate that HA was the main phase in the coatings. In addition, the strong band observed at 962 cm^{-1} corresponds to the fully symmetric stretching mode of ν_1 PO_4^{3-}.The sharpness of this band confirms the good crystallinity of HA coating [38].

Raman mapping was also carried out on the coatings to find out the homogeneity of the phases present in the coating (see supplementary figures). It can be observed that the HA phase is homogeneously distributed in the coatings with minor TCP components localized in specific area in the coatings.

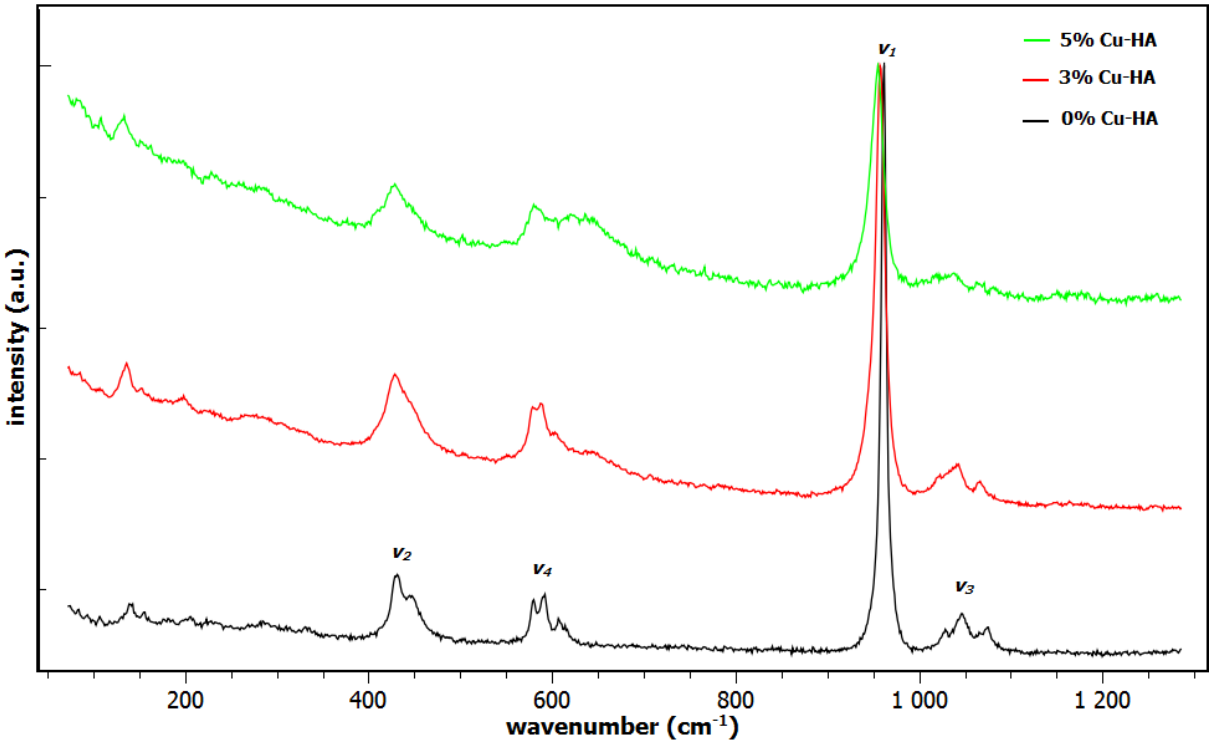

Figure 4: Raman spectra of SPPS Cu-HA coatings with different copper concentration

Raman spectra of 3% Cu-HA and 5% Cu-HA coatings present the same features as pure HA. However, the main band position was slightly red-shifted and clearly broadened (see Figure 5) which implies that the modification on the HA structure takes place on the phosphate groups (PO_4^{3-}). The measured full width at half maximum (FWHM) of the intense peak around 940-980 cm^{-1} associated to the ν_1 PO_4^{3-} vibrations shows significant increase having values of 7.089 cm^{-1}, 12.773 cm^{-1} and 17.027 cm^{-1} with increasing copper content. This broadening can be associated to the decrease of crystallinity due to the presence of other phases such as α- and β-TCP. In addition, a broadening in the 622-636 cm^{-1} region can be attributed to the presence of B_g vibrations of tenorite CuO in the coatings [39]. With increasing content of Cu, the

wavenumber of the symmetric stretching of PO_4^{3-} band decreases from 962 cm^{-1} down to 955 cm^{-1} which indicates a change in the PO_4^{3-} surrounding implying an increase of P-O bond distances. This increase signifies expansion in the unit cell of the HA structure which correlates to the unit cell volume increase in our Rietveld refinement results. This behavior can probably be linked to the insertion of Cu atoms interstitially in the HA structure which occurs on a site in the hexagonal channel that can affect the PO_4^{3-}groups leading to an isotropic increase in the HA unit cell volume. Previous studies described that copper ions was in the HA structure leading to the formation of linear O-Cu-O oxocuprate entities which resulted to the expansion of the unit cell volume [7].

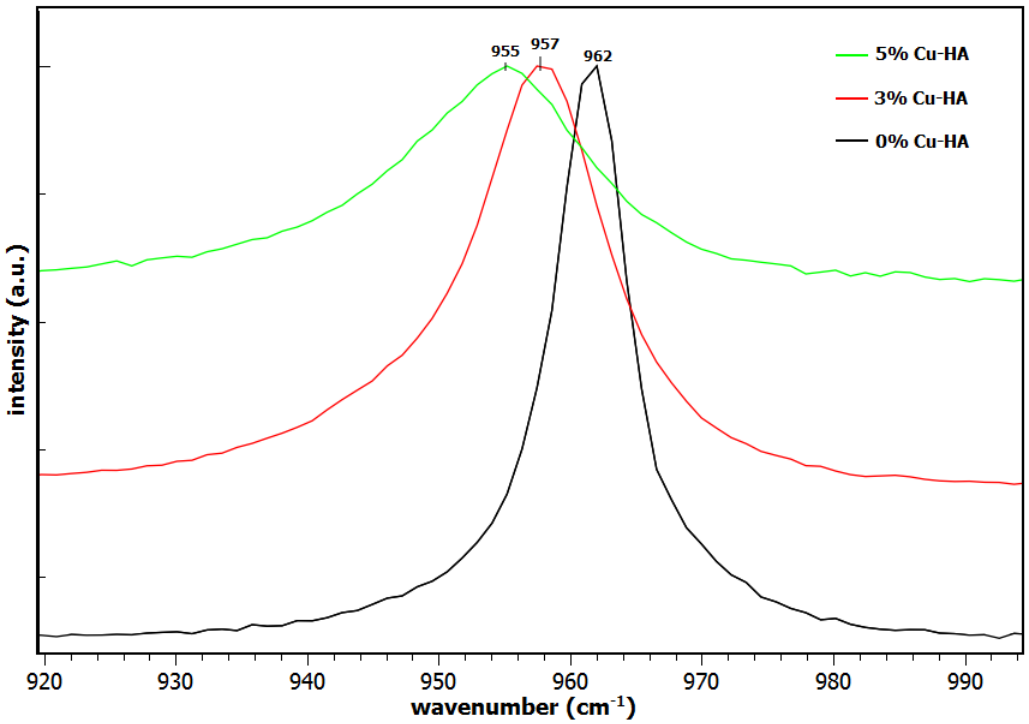

Figure 5: 900-1000 cm^{-1} region of Raman spectra of Cu-HA

3.6. Chemical analysis by inductively coupled plasma - atomic emission spectroscopy (ICP-AES)and X-ray photoelectron spectroscopy (XPS)

ICP-AES and XPS were carried out in order to quantify the concentration of copper element and determine the electronic state of the copper species in the coatings. One can observe from Figure 6 that the copper content in the coatings was increasing with increasing

copper dopant concentration which confirms a successful incorporation of copper ions into the HA structure. It should be noted that the coating was scraped off from the substrate and then subjected to ICP-AES characterization for quantitative elemental analysis. Calculation of calcium to phosphate ratio gives a value of 2.2, 2.1 and 1.9 and a calcium-copper to phosphate ratio of 2.2, 2.4 and 2.2 for pure HA, 3% and 5% Cu-HA coatings, respectively.The values obtained were non-stoichiometric, i.e., higher that 1.67, indicating the deposition of calcium-rich coating. This further confirms that no copper substitution has taken place. This non-stoichiometric ratio was also attributed to the phosphorous deficiency in the coatings which was probably due to the dissociation/volatilization of P_2O_5 at high temperatures [17].

On the other hand, XPS (see supplementary figures) results revealed the presence of Cu^{2+} cations and its corresponding satellite peaks observed at the range of 934-943 eV. Moreover, a strong peak at 932.63 eV is associated to the electronic state of Cu^{+} attributed to the reduction of Cu^{2+} at high temperatures above 1100ºC. This result confirmed that copper species inserted in the HA structure were Cu^{+}, and Cu^{2+} entities [7].

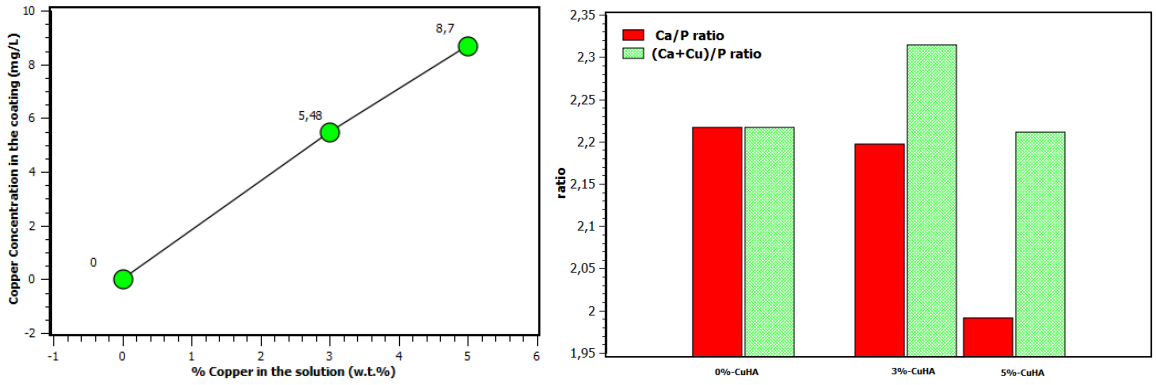

Figure 6 (left) Copper concentration in the deposited coating and (right) stoichiometric ratio of the coatings

4. Discussion

4.1. Influence of Cu concentration on the microstructure of the coatings

The SEM micrographs of the coatings show no particular changes on their morphology at the surface and cross-section upon doping of copper ions into the HA matrix. This

observation was expected due to minute concentration of copper added in the solution precursor feedstock used for spraying. The morphological characteristics of Cu-HA coatings in this present work are in good agreement with the study of Candidato *et al.* [17] on SPPS Zn-doped HA. Similarly, insertion of the copper ions into the HA lattice distorts the crystal structure of HA which hinder its crystallization as observed with the decreasing degree of crystallinity as the copper concentration increases. Consequently, the average crystallite sizes of all coating at various copper concentration remains in the range of nanometer scale, i.e. 83 nm to 118 nm which is favorable for bone regeneration application as it mimics the dimensions of the natural bones [32-33]. The production of nanoscale crystallite sizes can be attributed to the breaking up of the solution droplets into fine ones using SPPS process which resulted to full pyrolysis of the droplets as it penetrates into the plasma jet [40]. However, the maximum copper concentration to be incorporated in the HA lattice which preserves the dominance of HA phase in the coatings was 5 wt.% Cu due to the fact that the HA structure can only accommodate certain amounts of other ions in its lattice [17].

4.2. Copper incorporation mechanism

XPS result shows the electronic states of Cu^{+} and Cu^{2+} cations in the Cu-HA coatings confirming the successful incorporation of copper ions into the HA structure. The mechanism of copper incorporation in HA was presumed to be a substitution of copper ions on the *Ca(II)* sites which is characterized by a decrease in the lattice parameters and cell volume contraction of HA due to the smaller ionic radius of Cu^{2+} compared to the Ca^{2+}[10, 34, 41]. Contrary to the expected substitution mechanism, Rietveld refinement obtained from this present work shows a slight increase in the basal *a* lattice parameter along with the increase of the unit cell volume with increasing copper dopant concentration into HA. Moreover, ICP-AES results further solidifies our claim that no calcium site substitution has taken place due to the non-

stoichiometric Ca/P ratio, i.e., greater than 1.67 for all the coatings indicating that calcium-rich coating was being deposited.

In addition, Raman and IR spectra shows red-shifting and broadening of the peaks associated to the phosphate vibrations of HA with increasing copper concentration. Based on the results, copper ions could possibly be inserted in interstitial position inside the HA matrix along the hexagonal channel. This claim was in agreement with the crystallographic studies on Cu-doping into HA which reported interstitial insertion of Cu atoms at 2b Wyckoff site along the hexagonal channel leading to the formation of linear oxocuprate O-Cu-O entities in the HA structure [7, 35-36]. This possible copper ion insertion mechanism was favored due to high sintering temperature above 1100^{o}C of the plasma jet.

It has been reported that the formation of Cu-HA was a result of the transformation of α-TCP polymorph and copper-phosphate phases at temperatures above 1100^{o}C from the cooling process [7]. In here, in-flight particles traveling along the high temperature plasma jet may lead to the dehydroxylation of HA given by the equation:

$$Ca_{10}(PO_4)_6(OH)_2 \rightarrow Ca_{10}(PO_4)_6(OH)_{2-2x}O_x\square_x + xH_2O \uparrow \qquad \text{(Eq. 3)}$$

where $\square$ is the vacancy and x<1. The results in the phase transformation of HA into TCP and the formation of calcium copper phosphate phases that leads to the insertion of copper on the vacancies induce by the dehydroxylation process. The presence of TCP and CCP phases in XRD results which supports the transformation of HA together with the presence of Cu^{+} and Cu^{2+}cations in XPS confirms the incorporation of copper ions in the HA matrix producing coatings with chemical formula $\boldsymbol{Ca_{10}Cu_x(PO_4)_6(OH)_{2-2x}O_{2x}}$. However, the limitation on which copper ions are incorporated on the HA matrix was 5 wt.% of Cu in order to maintain HA as the dominant phase in the coatings.

On the other hand, comparing our calculated lattice parameters with SPPS Zn-doped HA coating using similar doping concentration shows values of $\boldsymbol{a}$ = 9.4113(6) Å and $\boldsymbol{c}$ =

6.8892(5) Å for Zn-doped HA compared with ***a*** =9.4280(3) Å and ***c*** = 6.8877(2) Å for Cu-HA suggesting a different insertion mechanism. Previous studies on SPPS Zn-doped HA coating reported interstitial insertion of linear O-Zn-O entity in the OH crystallographic site of HA inducing an increase in the lattice *c* parameters with no significant influence on the unit cell volume [17]. However, in this present study, the incorporation of the copper ions into the interstitial site along hexagonal channel shows increase in the lattice *a* parameters only and bring about an isotropic increase in the volume of HA unit cell (see Table 1). Furthermore, previous studies have reported that insertion of the linear O-Zn-O in the HA lattice attracts the adjacent phosphate groups but not with case of O-Cu-O oxocuprate [7]. Hence, the presence of O-Zn-O attracts the PO bands while O-Cu-O possibly repels the PO band leading to the expansion of the unit cell volume.

Furthermore, the transformation of HA into TCP's due to dehydroxylation also indicates that copper ion insertion might be localized in an interstitial site affecting the hydroxyl column as well. Related studies suggested that existence of ordered isolated [OCuO] units might be present along the channel [37-38].

5. Conclusion

Structural and microstructural investigation on the newly developed solution precursor plasma sprayed copper-doped HA with varied dopant concentration has been presented. No significant changes on the microstructural features on the surface and cross-section of the coatings were evident as copper content increases. A decrease in HA phase content from 93% to 14% and degree of crystallinity form 94% to 85% along with the increase of impurity phases were observed upon increasing the copper dopant concentration. RAMAN and IR spectra shows broadening and red-shifting of the phosphate bands with increasing copper dopant concentration due to the distortion in the HA structure brought about by the insertion of copper

ions. XPS results identified that the copper species incorporated in HA structure were Cu^{+} and Cu^{2+} ions. Rietveld refinements confirmed the increase of the lattice *a* parameter and expansion of the unit cell volume due to the incorporation of copper ions into the HA lattice.

These results evidenced that the incorporation mechanism of copper ions is probably an interstitial insertion along hexagonal channel of the HA structure. The insertion was induced by the dehydroxylation process of HA due to the high temperatures of the plasma jet. No calcium substitution has taken place contrary to the claims of some previous reports since SPPS process had deposited calcium-rich coatings as confirmed by the ICP-AES results.

In this study, 5 w.t% Cu is the maximum Cu quantity to be incorporated into the HA matrix keeping the HA phase the dominant phase in the coating. In-vitro characterization of the coatings under simulated body fluids, cytotoxicity and antibacterial testing will be conducted for the investigation of the feasibility of the SPPS Cu-HA coatings for biomedical application with added biofunctionality.

Acknowledgement

Romnick Unabia would like to acknowledge the Department of Science and Technology-Accelerated Science and Technology Human Resource Development Program (DOST-ASTHRDP) for the scholarship grant, and Department of Science and Technology - Philippine Council for Industry, Energy and Emerging Technology Research and Development (DOST-PCIEERD) for the financial grant. The authors acknowledges CarMaLim (IRCER, University of Limoges) platform for the equipment used in the characterization. Yann Launay, Richard Mayet, Julie Cornette, Sandra Blanchet and Etienne Laborde are also acknowledged for their help in the characterization of the coatings.

References

1. D. Campoccia, L. Montanaro, C.R. Arciola, The significance of infection related to orthopedic devices and issues of antibiotic resistance, *Biomaterials* 27 (2006), 2331-2339

2. Z. Radovanovic, B. Jokic, D. Velijovic, S. Dimitrijevic, V. Kojic, R. Petrovic, D. Janackovic, Antimicrobial activity and biocompatibility of Ag^{+}- and Cu^{2+}-doped biphasic hydroxyapatite/α-tricalcium phosphate obtained from hydrothermally synthesized Ag^{+}- and Cu^{2+}-doped hydroxyapatite, *Appl. Surf. Sci.* 307 (2014), 513-519
3. S. Shanmugan, and B. Gupal, Copper-substituted hydroxyapatite and fluoroapatite: synthesis, characterization and anti-microbial properties, *Ceram. Int.* 40 (2014) 15655-15662.
4. D. Bellucci, A. Sola, V. Cannillo, Hydroxyapatite and tricalcium phosphate composites with bioactive glass as second phase: state of the art an current applications, J. *Biomed. Mater. Res. A* 104A (4) (2016), 1030-1056
5. H.G. Hanumantharaju, H. K. Shivanand, K. P. Prashanth, K. Suresh Kumar, S.P. Jagadish, Study on hydroxyapatite coatings on biomaterials by plasma spray method, *Int. J. Eng. Sci. Tech.* 4 (9) (2012) 4152-4159
6. D. Shi, Introduction to Biomaterials, World Scientific Ltd., London, England (2005)
7. S. Gomes, C. Vichery, S. Descamps, H. Martinez, A. Kaur, A. Jacobs, J.M. Nedelec, G. Renaudin, Cu-doping of calcium phosphate bioceramics: From mechanism to the control of cytotoxicity, *ActaBiomaterialia* 65 (2018) 462-474
8. V. Stanic, S. Dimitrijevic, J. Antic-Stankovic, M. Mitric, B. Jokic, I.B. Plecas, S. Raicevic, Synthesis, characterization and antimicrobial activity of copper and zinc-doped hydroxyapatite nanopowders, *Appl. Surf. Sci.* 256 (2010) 6083-6089
9. C.K. Sen, S. Khanna, M. Venojarvi, P. Trikha, E.C. Ellison, T.K. Hunt and S. Roy, Copper-induced vascular endothelial growth factor expression and wound healing, *Am. J. Physiol. Heart Circ. Physiol.* 282 (2002) H1821-1827
10. F.E. Imrie, J.M.S. Skakle and I. Gibson, Preparation of Copper-doped Hydroxyapatite with varying x in the composition $Ca_{10}(PO_4)_6Cu_xO_yH_z$, *Bioceram. Dev. Appl.* (2013) S1:005
11. T.N. Kim, Q.L. Feng, J.O. Kim, J. Wu, H. Wang, G.C. Chen, F.C. Cui, Antimicrobial effects of metal ions (Ag^{+}, Cu^{2+}, Zn^{2+}) in hydroxyapatite, *J. Mater. Sci.: Mater. Med.* 9 (1998) 129-134
12. A.V. Lyasnikova, O.A. Markelova, O.A. Dudareva, V.N. Lyasnikov, A.P. Barabash, S.P. Shpinyak, Comprehensive characterization of plasma-sprayed Coatings based silver- and copper-substituted Hydroxyapatite, *Powder Metall. and Metal Ceram.*55 (2016) 5-6
13. A. Mariappan, P. Pandi, N. Balasubramanian, R. RajeshwaraPalanichamy, K. Neyvasagam, Structural, Optical and Antimicrobial Activity of Copper and Zinc Doped

Hydroxyapatite Nanoparticles using Sol-Gel Method, *Mech. Mater. Sci. Eng. J.*, *Magnolithe* 9 (1) (2017) 1-5

14. Y. Li, J. Ho, C.P. Ooi, Antibacterial efficacy and cytotoxicity studies of copper (II) and titanium (IV) substituted hydroxyapatite nanoparticles, *Mater. Sci. Eng. C* 30 (2010) 1137–1144
15. B.R. Stern, Essentiality and toxicity in copper health risk assessment: overview, update and regulatory considerations, *J. Toxicol. Environ. Health Part A* 73 (2010) 114-127
16. S. Jin, L. Ren, K Yang, Biofunctional Cu containing biomaterials: a new way to enhance bio-adaptation of biomaterials, *J. Mater. Sci. Tech.* 32 (2016), 835-839
17. R. Candidato, R. Sergi, J. Jouin, O. Noguera and L. Pawłowski, Advanced microstructural study of solution precursor plasma sprayed Zn doped hydroxyapatite coatings, *J. Eur. Ceram. Soc.* 38 (2018) 2134–2144
18. R. Unabia, S. Bonebeau, R. Candidato, Jr., L. Pawłowski, Preliminary Study on copper-doped hydroxyapatite coatings obtained using solution precursor plasma spray process, *Surf. Coat. Tech.* 353 (2018), 370-377
19. Bruker AXS, TOPAS V4.2: General Profile and Structure Analysis Software for Powder Diffraction Data, B.A. Karlsruhe . 2009
20. E. Landi, A. Tampieri, G. Celloti, S. Sprio, Densification behaviour and mechanisms of synthetic hydroxyapatites, *J. Eur. Ceram. Soc.* 20 (2002) 2377-2387
21. R. Unabia, J.C. Piagola, J.R. Guerrero, R. Vequizo, J. Gambe, M.K. Vequizo, B.R. Sambo, Synthesis and characterization of nanocrystalline hydroxyapatite and biphasic calcium phosphate using $Ca(OH)_2$ and $(NH_4)H_2PO_4$, *Phys. Status Solidi C* 12 (6), (2015), 572-575
22. G.K. Williamson and W.H. Hall, X-ray line broadening from filed aluminum and wolfram, *Acta Metall.* 1(1) (1953), 22-31
23. H.M. Rietveld, A profile refinement method for nuclear and magnetic structures, *J. Appl. Cryst.* 2 (1969) 65–71
24. V. Petricek, M. Dusek, L. Palatinus, Crystallographic computing system JANA2006: general features, *Z. Kristallogr.* 229 (5) (2016) 345–352
25. P. de Wolff, TechnischPhysischeDienst, Delft, The Netherlands, ICDD Grant-in-Aid, CAS# 1306-06-5
26. P. de Wolff, TechnischPhysischeDienst, Delft, The Netherlands, ICDD Grant-in-Aid, CAS# 7758-87-4
27. Natl. Bur. Stand. (U.S.), Monogr. 25, 12 (1975), 17, CAS # 1306-01-0
28. B. Lazoryak, S. Khasanov, Moscos State University, Russia, ICDD Grant-in-Aid (1994)

29. H. McMurdie, M. Morris, E. Evans, B. Paretzkin, W. Wong-Ng, C. Hubbard, *Powder Diffr.*1 (1986), 266, CAS# 1305-78-8
30. J. Langford, D. Luoer, High-resolution powder diffraction studies of copper (II) oxide*J. Appl. Crystallogr.* 24 (1991), 149
31. International Organization for Standards, Implants for Surgery – Hydroxyapatite. Part 2: Coatings of Hydroxyapatite, BS ISO 13779-2:2000, 2000
32. P. Ducheyne, K. Healy, D.E. Hutmacher, D.W. Grainger, C.J. Kirkpatrick, Comprehensive Biomaterials, Vol. 1, Elsevier, Amsterdam, The Netherlands, 2011, 329-338
33. M.P. Ferraz, F.J. Monteiro, C.M. Manuel, Hydroxyapatite nanoparticles: A review of preparation methodologies, *J. Appl. Biomater. Biomech.* 2 (2004) 74-80
34. R.D. Shannon, C.T. Prewitt, Revised effective ionic radii and systematic studies of interatomic distances in halides and chalcogenides, *ActaCryst. A* 32 (1976) 751–767
35. G. Renaudin, S. Gomes, and J-M. Nedelec, First-row transition metal doping in calcium phosphate bioceramics: a detailed crystallographic study, *Mater.* 10 (2017), 92-113
36. A. Karpov, J. Nuss, M. Jansen, P. Kazin, Y. Tretyakov, Synthesis, crystal structure and properties of calcium and barium hydroxyapatites containing copper ions in hexagonal channels, *Solid State Sci.* 5 (2003), 1277-1283
37. M. Zykin, A. Vasiliev, L. Trusov, R. Dinnebier, M. Jansen, P. Kazin, Solid state solubility of copper oxides in hydroxyapatite, *J. Solid State Chem.* 262 (2018), 38-43
38. H. Li, B.S. Ng, K.A. Khor, P. Cheang, T.W. Coyle, Raman spectroscopy determination of phases within thermal sprayed hydroxyapatite splats and subsequent in vitro dissolution examination, *Acta Mater.* 52 (2004), 445-453
39. M. Rashad, M. Rusing, G. Berth, K. Lischka, and A. Pawlis, CuO and Co_3O_4 nanoparticles: synthesis, characterizations, and Raman spectroscopy, *J.Nanomater.* 2013 (2013), 1-6
40. R. Unabia, R. Candidato, Jr., L. Pawłowski, Current Progress in Solution Precursor Plasma Spraying of Cermets: A Review, *Metals* 8 (2018), 420
41. M. Othmani, H. Bachoua, Y. Ghandour, A. Aissa, M. Debbabi, Synthesis, characterization and catalytic properties of copper-substituted hydroxyapatite nanocrystals, *Mater. Res. Bull.*97 (2018), 560-566

Supplementary Figures:

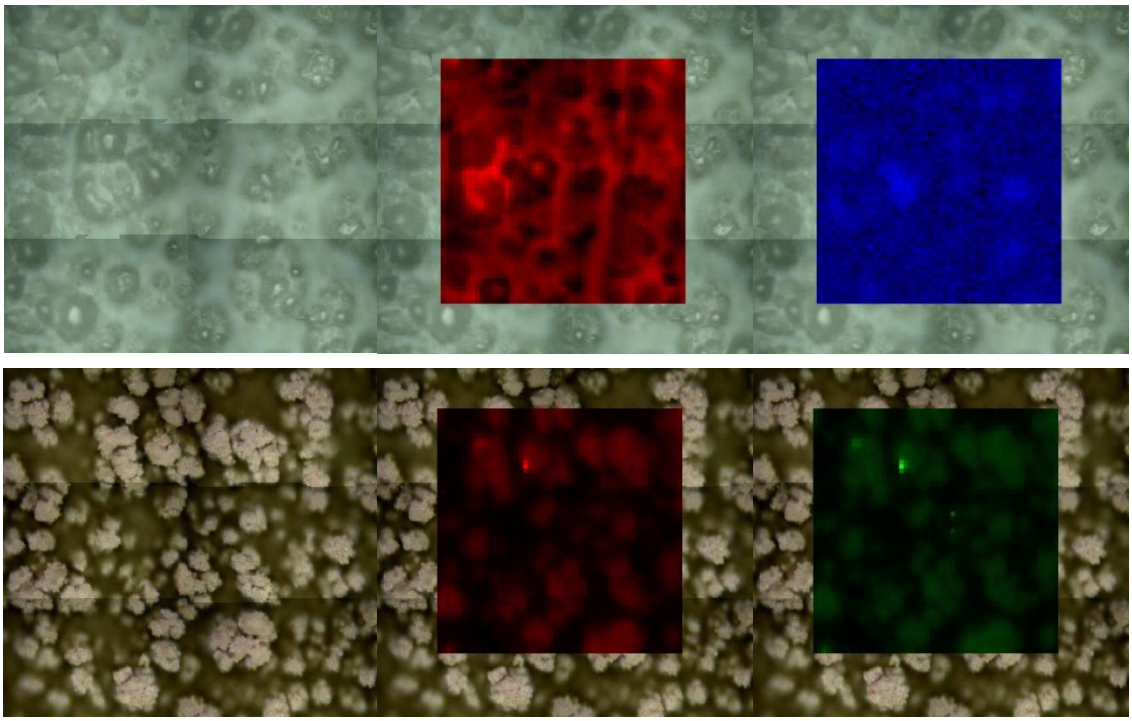

Figure 1 Raman mapping of pure HA and 5% Cu-HA showing (red) HA phase, (blue) TTCP phase, and (green) TCP phase.

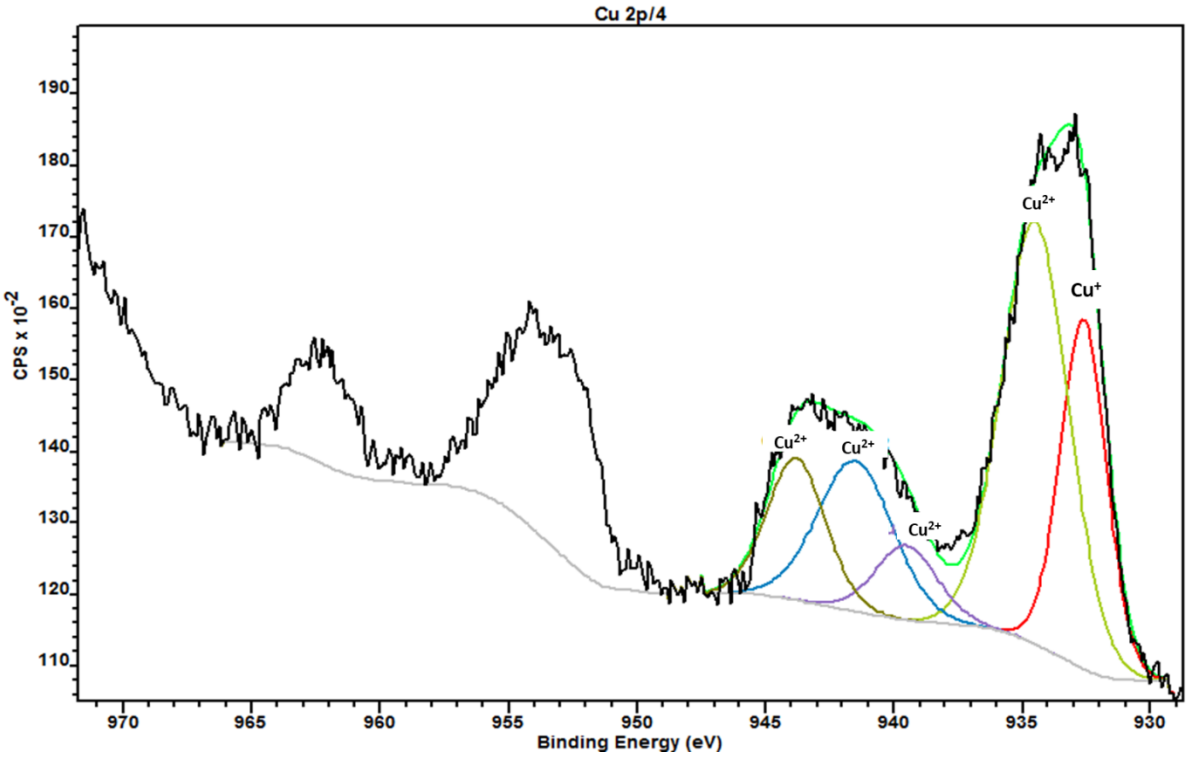

Figure 2 XPS result showing the binding energy of the Cu 2p spectrum for 5% Cu-HA